Journal of Physics and Chemistry of Solids 201 (2025) 112657

Contents lists available at ScienceDirect

Journal of Physics and Chemistry of Solids

journal homepage: www.elsevier.com/locate/jpcs

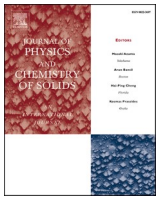

Comprehensive analysis of structural, dielectric, magnetic properties in self-propagating high-temperature (SHS) prepared lead iron niobate

Tanveer Quazi [a], Shahin Sayyad [b,*], Vishwajit M. Gaikwad [c]

[a] Anjuman College of Engineering & Technology, Nagpur, 440001, Maharashtra, India
[b] Department of Physics, Shri Shivaji Education Society Amravati's Science College, Nagpur, M.S, India
[c] Department of Physics, Amolakchand Mahavidyalaya, Yavatmal, M.S, India

ARTICLE INFO

Keywords:
Multiferroics
Non-relaxor
Nono-electronics
Rietveld

ABSTRACT

Lead iron niobate, $Pb(Fe_{1/2}Nb_{1/2})O_3$ (PFN), was synthesized via a self-propagating high-temperature synthesis (SHS) technique. The SHS process achieved pyrochlore-free monoclinic perovskite (space group Cm) at room temperature, transitioning to cubic symmetry (Pm3 m) above 380 °C, as confirmed by high-temperature XRD (HT-XRD). Lattice contraction with rising temperature revealed negative thermal expansion (NTE), driven by Pb^{2+} vibrational modes and octahedral tilting. Sintering at 800 °C (PFN-8-3) eliminated residual pyrochlore phases ($Pb_2Fe_4Nb_4O_{21}$) and enhanced relative density to 98 %, compared to 80 % for samples sintered at 700 °C (PFN-7-2). Dielectric studies identified a diffuse phase transition (DPT) near 105–115 °C, with permittivity reaching ~18,600 (1 kHz) for PFN-8-3, attributed to grain densification and reduced porosity. Frequency-independent T_m and Debye-like relaxation confirmed non-relaxor behavior, linked to ordered Fe^{3+}/Nb^{5+} B-site cation distribution. Electron density mapping via Fourier analysis highlighted Pb-dominated charge density (~69 e/Å^3), with Fe/Nb contributions (~29–32 e/Å^3), aligning with X-ray scattering trends. Magnetic hysteresis loops revealed weak room-temperature ferromagnetism, intensifying at higher sintering temperatures (coercivity ~80 Oe, remnant magnetization ~0.12 emu/g for PFN-8-3). The coexistence of ferroelectricity and ferromagnetism underscores PFN's potential in multifunctional devices, while the SHS route offers a rapid, energy-efficient pathway to phase-pure perovskites. This work bridges synthesis optimization, structural dynamics, and functional performance, advancing PFN's applicability in high-density capacitors, magnetoelectric sensors, and thermal management systems.

1. Introduction

Lead Iron Niobate (PFN), a Pb-based complex perovskite with the general formula $[A(B_{1/2}B'_{1/2})O_3]$, has garnered significant attention "due to its high potential for diverse applications, remarkable relative permittivity, and low sintering temperature" [1–6].This material exhibits promising applicability across a wide range of fields, including nano-electronics, automation, control processes, robotics, micro-mechatronics, material processing, aerospace engineering, automotive industries, defence technology, medical and biotechnology, multilayer ceramic capacitors (MLCC), actuators, memory devices, pyroelectric sensors, and more [7–13].

At room temperature, PFN crystallizes in a polar rhombohedral structure with R3m symmetry, undergoing a diffused phase transition (DPT) at approximately 387 K to a cubic Pm3 m symmetry [14]. Diffraction analyses reveal that PFN adopts a monoclinic perovskite structure with the 'Cm' space group at room temperature [15,16]. The diffuse phase transition observed in PFN is attributed to the disordered arrangement of B-site cations within the perovskite lattice [17,18]. Recently, the classification of PFN as a relaxor or non-relaxor material has been a subject of debate, further highlighting its complex and intriguing nature [19].

PFN has been synthesized through various routes, including sol-gel [4], reaction sintering [20], molten salt synthesis [21], the columbite method [22], the hydroxide route [23], conventional solid-state synthesis [24–28], ball milling [29], and wet chemical methods [30]. These techniques aim to achieve a pure perovskite phase with a high dielectric constant. However, the synthesis of PFN is often plagued by challenges, such as the formation of low-dielectric pyrochlore phases (e.g. $Pb_3Nb_4O_{13}$ or $Pb_2Nb_2O_7$) due to PbO loss [31,32]. These issues

* Corresponding author.
E-mail addresses: shahinsayyed87@gmail.com, shahin.sayyad@sscnagpur.ac.in (S. Sayyad).

https://doi.org/10.1016/j.jpcs.2025.112657
Received 9 January 2025; Received in revised form 22 February 2025; Accepted 25 February 2025
Available online 27 February 2025

necessitate high sintering temperatures, prolonged processing times, and multiple calcination and sintering steps, often resulting in larger particles with significant inhomogeneity [33]. Table 1 summarizes the various synthesis conditions employed for PFN and their impact on dielectric properties.

In recent years, Self-sustaining High-temperature Synthesis (SHS) has emerged as a promising technique for producing multicomponent oxide ceramic powders without the need for intermediate calcination steps [34–42]. SHS is a material production method that leverages the heat generated during exothermic chemical reactions to sustain the synthesis process. This technique is particularly effective for producing intermetallic and composite materials. The rapid reaction rates and steep thermal gradients inherent to SHS result in high-density materials with well-defined crystal structures.

Motivated by these advancements, this study focuses on the synthesis of pyrochlore-free PFN perovskites in a single step using the SHS technique. The chemistry of the synthesis route is thoroughly investigated, and the ambiguity surrounding the crystal structure of PFN is resolved through Rietveld refinement. The structural findings are correlated with morphological and dielectric studies conducted at varying temperatures. Additionally, the relaxor and non-relaxor behaviour of PFN is explored, providing deeper insights into its phase transition dynamics and dielectric properties. This work aims to contribute to the understanding of PFN's synthesis-structure-property relationships, paving the way for its optimized application in advanced technologies.

2. Experimental method

The starting materials include $Fe(NO_3)_3.9H_2O$ (99 %, Merck), $Pb(NO_3)_2$ (Merk, 99 %), and Nb_2O_5 (Sigma-Aldrich, 99.5 %) as cation precursors, while urea, $CO(NH_2)_2$ (Merck, 99 %), serves as the fuel. The stoichiometric ratio is maintained according to the following chemica equation.

In order to synthesis, the perovskite via the SHS technique, urea is employed as the fuel. Crystalline $Pb(NO_3)_2$ serves as the lead source, while $Fe(NO_3)_3.9H_2O$ is utilized as the iron source. Nb_2O_5 is incorporated as the niobium source. As noticed, niobium is not available as a nitrate salt; rather, the oxide serves as a precursor, despite its lack of contribution to the SHS reaction [38]. The inclusion of inert oxides in the precursor mixture does not markedly influence its redox properties; however, it necessitates the addition of supplementary fuel. During the process, Nb_2O_5 stays inert; the urea content simply needs to balance the lead and iron nitrates. When the propellant chemistry criterion is applied directly, the stoichiometric composition of the redox mixture is determined to be 31.84 mol of urea, 2 mol of $Pb(NO_3)_2$, 1 mol of $Fe(NO_3)_3$, and 0.5 mol of Nb_2O_5.Reactant in the molar ratios of 2:1:0.5:31.84 is used to prepare the sample batches; it ignites easily at 500 °C but not very significantly.

A homogeneous mixture was achieved by thoroughly stirring the initial precursors for 15 min after mixing them with 50 mL of double-distilled water. The ideal heating temperature for the homogeneous solution was 250 °C. Long-term frothing and thickening of the liquid were followed by ignition and the development of nitrate fumes, which signalled the start of combustion. In order to complete the combustion reaction and produce a reddish-brown product, the solidified PFN was heated to 500°C for 10 min in a muffle furnace. Finally, 5 tons/cm^2 of pressure was used to compress the powder into pellets. The resulting pellets are sintered at 700°C for 2 or 3 h; they are referred to as PFN-7-2 and PFN-7-3, respectively. The sintered samples at 800°C are referred to as PFN-8-2 and PFN-8-3 in whole text.

3. Material characterization

A structural study on samples was carried out by X-ray powder diffraction (XRD) using Cu-Kα_1 ($\lambda \approx 1.5406$ Å) radiation, with the help of a PANalytical X-ray powder diffractometer at 40 kV and 30 mA. Structural studies are also carried out at high temperatures of 50, 110, 150, and 200°C under vacuum (10^{-6} torr) using HTK-16, a high-temperature attachment to XRD (Anton Parr, Austria). The unit cell parameters are refined by a least squares method using the *Powder* software [43]. *Raw* XRD patterns are refined using the Rietveld refinement method via *FullProf software*. Particle size analysis of PFN was carried out using CM200 TEM (Transmission Electron Microscopy). The surface morphology of sintered samples was examined by a scanning electron microscope (JEOL: JSM-6380 Analytical SEM) equipped with an electronic probe analyzer system (accelerating voltage 30 kV. To provide good ohmic connections, platinum was applied to the samples. An Impedance analyser HP4192ALF was used to determine the dielectric constant, εr and dissipation factor, tanδ at various frequencies between 10 Hz and 1000 kHz in the temperature range of 25–200°C. The temperature was controlled with an accuracy of ±1°C by using a Eurotherm temperature controller.

4. Result and discussion

4.1. Structural studies

Fig. 1(i) (a, b, c, d) shows the XRD patterns of PFN-7-2, PFN-7-3, PFN-8-2, and PFN-8-3 samples, respectively. As seen in Fig. 1(a and b), the pyrochlore phase $Pb_2Fe_4Nb_4O_{21}$ (JCPDS 50–0445) at 29.2° is detected for 700°C. PFN pyrochlore phase vanished when the sample was sintered at 800°C. The (110) peak of XRD pattern for samples PFN-8-2 and PFN-8-3 confirms the perovskite phase (Fig. 1(c &d)). The relative percentage of perovskite to pyrochlore phase of PFN is

Table 1
Comparision the dielectric properties of PFN-ceramic material.

Sytnehsis route	Synthesis Condition	Phase Content	Structure	Tc (K)	Dielectric constant (frequency)	Loss Tangent	Ref.
Sol-Gel	Sintered 1373K for 4h,	Perovskite	Rhombohedral	370	~25,000 at T_c (100 kHz)	0.35 at T_c	[4]
Solid state	Calcined at 1072K for 2h, hot pressed at 1243K for 2.5h at 10 Mpa in air	Perovskite	Rhombohedral (R3m)	380	2570 at RT (100 kHz)	0.0136 at RT (100 kHz)	[18]
Solid state	Sintered at 1323 K for 1h	Pyrochlore + perovskite		383	800 at T_c (100 kHz)	0.5 at T_c	[19, 20]
Solid state	Calcined at 1273 K	Rhom. perovskite	Rhombohedral (R3m)	380	~2500 at RT (100 kHz)	———	[21]
Single crystal		Rhom perovskite	Rhombohedral (R3m)	–	750 at RT (1 MHz)	0.05 at RT (1 MHz)	[22]
Semiwet hydroxide	Sintered at 1273 K for 3h with $PbZrO_3$ packing powder	NA	–	383	18,000 at T_c~4500 at RT	0.3 at RT loss tangent dip ~ T_c	[23]
Mechano chemical		NA	–	385	22,000 at T_c (1 kHz)	0.4 at Tc	[29]
Chemical Wet Technique	Sintered at 1298K -1348K for 2h	Pyriocholre + Perovskite	Tetragonal (P4mm)	370–378	9774-15812 at T_c and 4207–7753 at RT	0.148-0.265 at RT and 0.208-0.381 at Tc	[30]

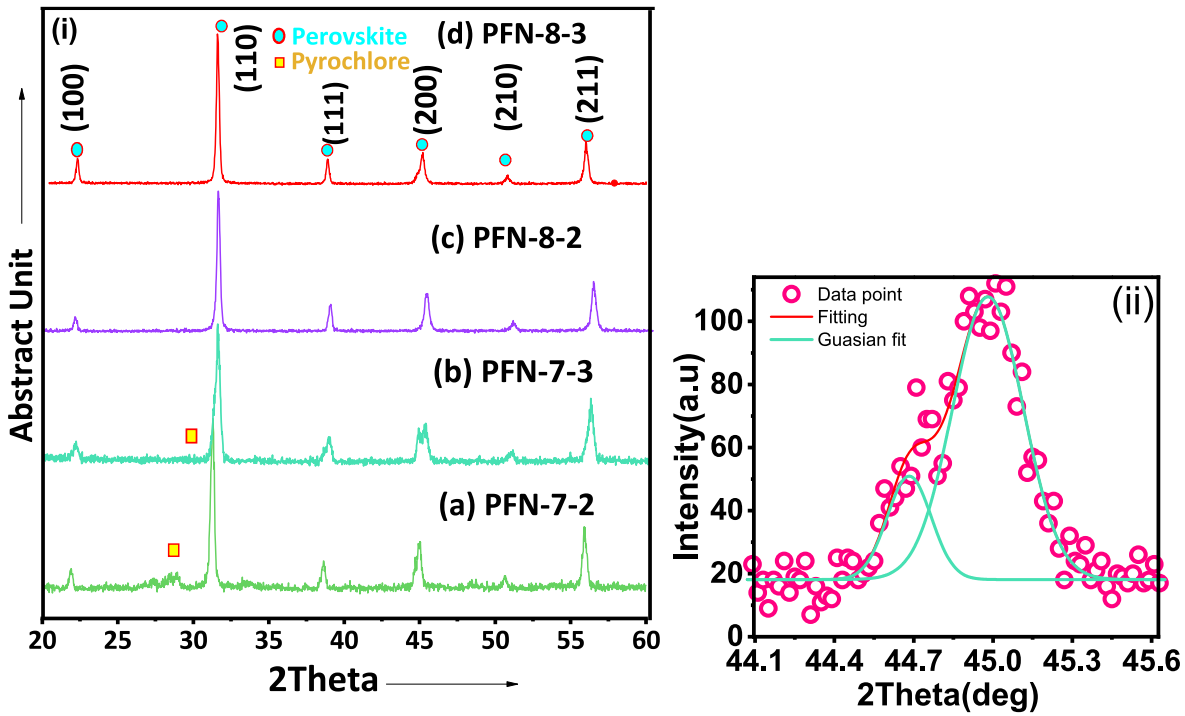

Fig. 1. (i) XRD pattern of PFN of samples; a) PFN-7-2 b) PFN-7-3 c) PFN-8-2 d) FN-8-3 and (ii) XRD pattern of PFN for slow scanned (0.6 deg/min) at 45° experimental circle (o) and fitted (solid line) of (200) peak for sintered at the 800°C for 3h

determined by calculating the intensity ratio of the major reflection peak of perovskite to the pyrochlore phase peak of XRD patterns using equation [44]. $Perovskite\ phase(\%) = \frac{I_{perov}}{I_{pesov} + I_{pyro}}$, here I_{perov} and I_{pyro} are the intensities of major reflection peaks of the perovskite and pyrochlore phase, respectively. The relative percentages of both phases are tabulated in Table 2. XRD patterns of samples PFN-8-2 and PFN-8-3 are well matched with the JCPDS data (file no. 0.032–0522) that confirms the single-phase monoclinic structure with *Cm* space group. The apparent density of all PFN samples was determined by the Archimedes principle [45], and relative density with porosity is calculated. It is observed that, relative density of PFN samples is enhanced with the sintering temperature and time, as shown in Table .2. A high density of about 98 % was achieved for the sample, PFN-8-3.

The slow acquisition (0.6 deg/min) of XRD pattern of PFN at room temperature shows the splitting in the perovskite reflection peaks corresponding to Bragg angle 45° as shown in Fig. 1 (ii). It is reported that PFN has either rhombohedral or monoclinic structure at room-temperature [31]. In rhombohedral structure, the reflection peak (200) has to be singlet, but for monoclinic symmetry, the peak splits into doublet. The peak that corresponds to (200) is deconvoluted, and it is quietly fitted with two peaks by using a Gaussian function that confirms the monoclinic symmetry (inset Fig. 2b).

The raw XRD pattern of PFN is refined by the Rietveld method using

Table 2
A comparison of perovskite phase, density, porosity and for PFN prepared by changing the preparative parameters sintering temperature and time.

Sr. No	Sample name	[a]T_{sinter} (°C)	#t_{sinter} (Hrs)	% of Perov phase	Relative density (%)	Porosity (%)
1.	**PFN-7-2**	700	2	94	80	20
2.	**PFN-7-3**	700	3	100	88	12
3.	**PFN-8-2**	800	2	100	90	10
4.	**PFN-8-3**	800	3	100	98	2

t_{sinter} for sintering time.
[a] T_{sinter} for sintering temperature.

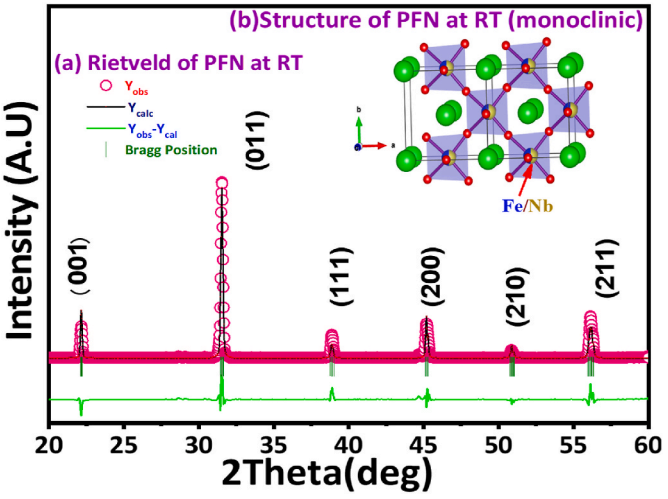

Fig. 2. (a) Rietveld analysis of XRD pattern of PFN at RT (open circles). (b) Structure of PFN (monoclinic).

the monoclinic structure of the 'Cm' space group [46], as shown in Fig. 2 (a and b). The solid line represents the simulated data. Vertical lines indicate Bragg peak positions, and blue lines indicate the difference between observed and simulated data. The excellent fitting over wide'd' spacing manifests the good quality data of PFN. From first-principles calculations for Pb-containing perovskite, it has been reported that Pb ions tend to avoid cube faces with high-valence ions and displace toward cube faces with low-valence ions [47]. The apparent large thermal parameter of Pb ions relative to Fe/Nb causes the structural disorder of PFN as observed by x-ray fluorescence holography. This is caused by a coupling of large static disorder with thermal displacement [48,49].

X-ray diffraction (XRD) yields two kinds of information: the first is about the unit cell's crystal structure, size, and shape; the second is the electron density distribution (EDD) throughout the unit cell, which is

obtained by reflecting a different X-ray wave from parallel planes of electron density. EDD can be reconstructed from accurate X-ray diffraction data by a sequence of intricate data reduction and processing techniques [50]. To observe electron density mapping and comprehend the distribution of electron density within the PFN unit cell, utilise the G-Fourier program 04.06, which is a component of the *FullProf suite* toolbar. To determine the locations of the atoms that make up the compound's constituent elements within the unit cell, the electron density analysis is useful. The Fourier transform of the geometric structural component applied to the entire unit cell is the electron density [51]. Output structure factor file (.inp), which is obtained after XRD data refinement, was used for electron density mapping. A two or three dimensional (2D) Fourier map is used to depict the electron scattering density. As a periodic function of position, the electron density reaches its maximum at the location of an atom and falls to a minimum value in the space between them. In this instance, a region with a high electron density is represented by orange, while a region with a low electron density is represented by blue. 2D-Fourier maps are frequently created as contours to show the electron density distribution surrounding each atom of the compound's constituent parts in order to comprehend the chemical bonding and charge transfer in the PFN [Pb($Fe_{1/2}Nb_{1/2}$)O_3] complex. A significantly heavier element is present in the unit cell if the electron density curves are thick and dense. In contrast, the 3D-Fourier maps show a single electron density level surrounded by a chicken-wire-like matrix. Fig. 3 shows a well-defined electron density distribution along [x, y, 0], [0, y, z], and [x, 0, z] directions within the Fourier limit 1 Å region of the PFN unit cell. Contours represent the region of positive electron density distribution. The distribution of electrons in the valence 2s and 2p orbitals may be responsible for the contours surrounding the O. In Fig. 3, the contour with the coloured area enclosing the Fe/Nb and O shows the electron density levels, while the blue contour shows the zero-level density contour. The

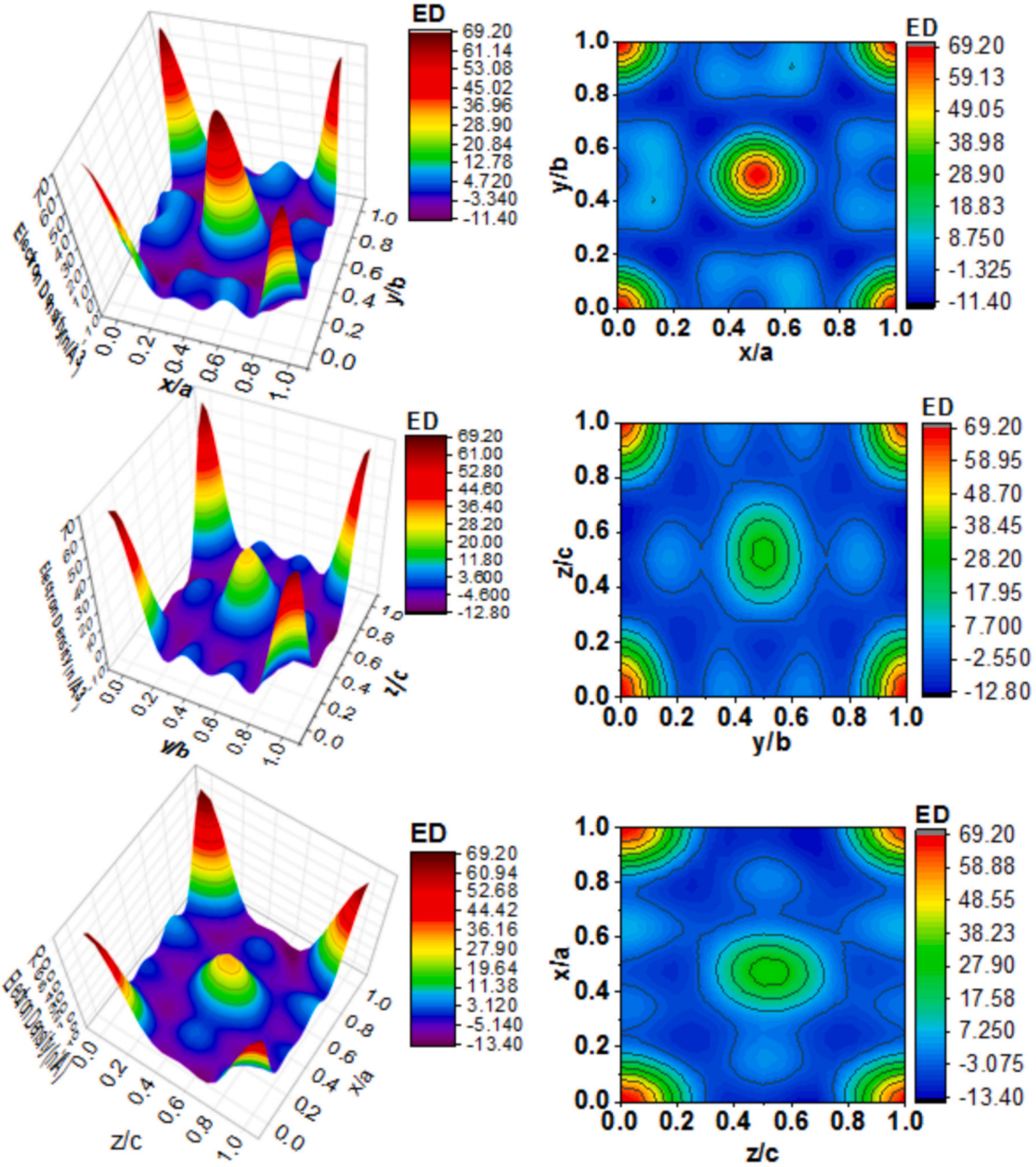

Fig. 3. Two and three dimensional electron density contour map on the xy, yz, zx-plane of monoclinic Pb($Fe_{0.5}Nb_{0.5}$)O_3 [PFN].

maximum levels of density of electron are found around Pb atoms in all directions (as shown in Fig. 3). The scattering of X-rays is determined by the number of electrons surrounding the atom. Since Nb atoms have more electrons than Fe atoms, as is well known, Nb should scatter more X-rays than Fe. The maximum electron density distribution values of Pb are 69e/Å^3 along all planes [shown by red colour] an along xy, yz, and zx directions, respectively, meaning that the peaks corresponding to Nb are more intense than those of Fe (Fig. 3). Distribution of electron density around Nb atom (~69 e/Å^3 along xy-direction) (indicate orange red) and Fe atom (~29 e/Å^3 along yz, ~32 e/Å^3, along zx direction) (indicate orange colour) is less than that of Pb. This is due to the fact that the number of electrons for the Nb atom is only 2, 8, 18, 12, and 1 for K, L, M, N, and O shells (for Fe, 2, 8, 14, and 2 for K, L, M, and N), while the number of electrons for the Pb atom is more than the Nb/Fe atom i.e., 2, 8, 18, 32, 18 & 4 for K, L, M, N, O, and P shells [52–54]. In order to reveal the temperature dependent structural transition, the high temperature XRD data of PFN at the temperatures of 50, 110, 150, and 200°C are obtained.

The Rietveld refinement is implemented to all the samples, the shifting and splitting of prominent Bragg reflections occur between 56° to 56.4°, which indicate the structural phase transitions from monoclinic (Cm) to cubic (m3m) within the temperature range 25°C and 250 °C. There was no indication of the 80 °C phase reported by other authors (Brunskill et al., 1981; Brunskill ***et al.,*** 1982) when temperature changes from 50 °C to 250 °C (Fig. 4(b, c)) [55,56]. The XRD patterns recorded in temperature range (110°C–250°C) show cubic structure and falls within same space group *(Pm3 m)*. The cell parameters of PFN sample within this temperature range decrease with escalating the temperature, hence, the reduction in cell volume with temperature is observed for cubic structure falls within same space group *(Pm3 m)*. The volume of PFN material changing with the variation of lattice parameters from 5.7 Å to 4.1 Å shows the negative thermal expansion (NTE). In NTE material contracts rather than expands as temperature increases. This behaviour is generally due to specific atomic interaction and vibrational modes, often involving transverse vibrations or rigid unit modes. These movements allow atoms to pull closer together as they vibrate more intensely with increasing temperature, reducing the overall volume. Thus, at higher temperatures, the structure becomes cubic (a = b = c = 4.1 Å) as shown in Fig. 5.

4.2. Morphology of as-sythesized and sintered PFN

The scanning electron microscope (SEM) and transmission electron microscopy (TEM) images of as-synthesized PFN powder are displayed in Figs. 6 and 7, respectively. Initially as-synthesized PFN exhibits highly agglomerated, irregular, and randomly distributed particles. The particle size of the oval-shaped crystalline phase varying from 50 to 70 nm was observed by TEM as shown in Fig. 7. The reaction residues, which could get removed by calcining at 500°C (see Fig. 6(a)) and sintered at 700°C–800°C, yield the pure crystalline phase of PFN spherical-shaped fine-scale grains. The SEM images of the fractured surface of PFN pellets sintered at 700°C and 800°C are taken, but only the 800°C image is shown in Fig. 6(b). Both samples at 700°C and 800°C exhibit highly dense regions. Grain size was determined by manual image analysis by matching digital pixel scale across each grain. The morphology of PFN-7-3 and PFN-8-3 samples shows nanoparticles of size <100 nm is aggregated into grains of size in the micrometer range. The sample sintered at 700°C exhibits an average grain size of 1.5 μm, and for the sample sintered at 800°C, the average grain size is found to be ~3 μm [Fig. 6(b)]. The density-dependent grain sizes of various synthesis routes are given in Table 3 [28,29,33,57,58]. In the examining PFN variations in density and grain size can significantly impact on the electrical and ferroelectric properties. The density influenced by factors like the sintering temperature and duration, where higher temperatures typically

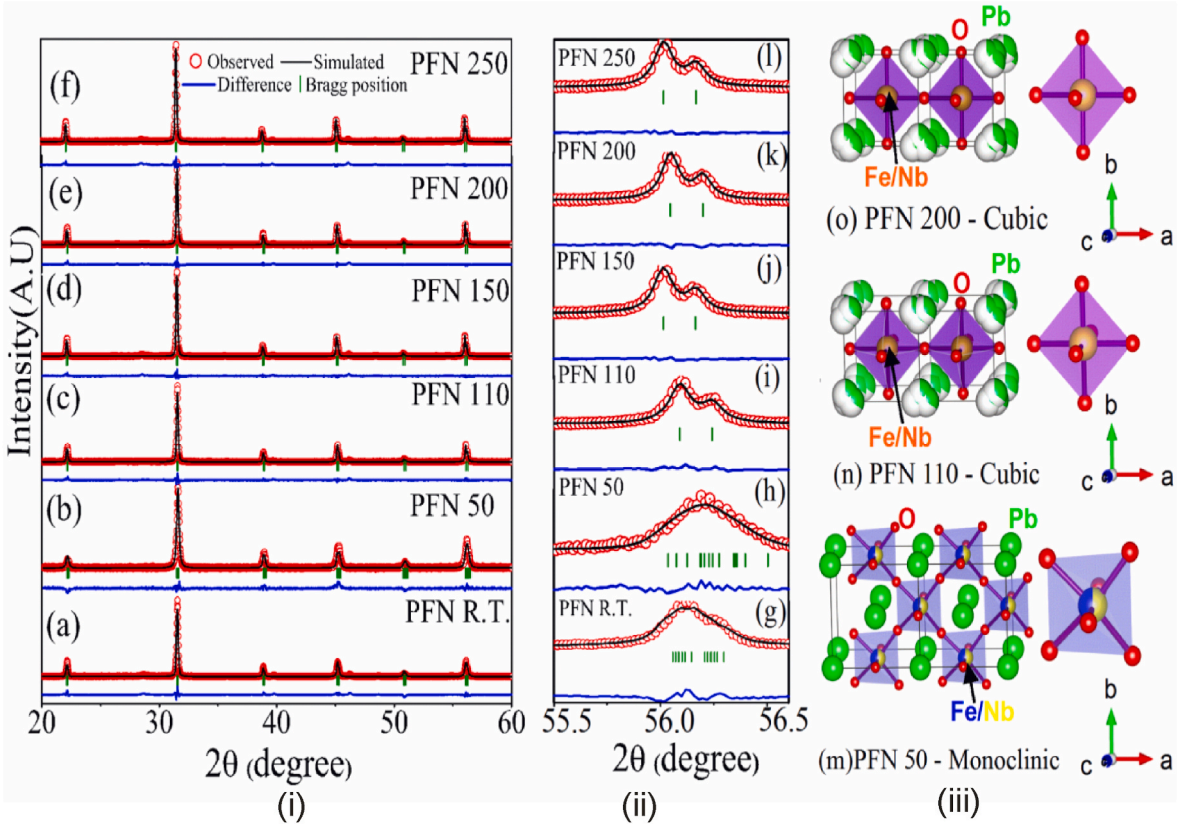

Fig. 4. (i)Rietveld analysis of High temperature XRD (HT-XRD) pattern (a–f) (ii) HT-XRD of PFN RT, 50, 110,150,200,250°C at 56(degree)(g-l)and (iii) modified structure from monoclinic to cubic(m-o).

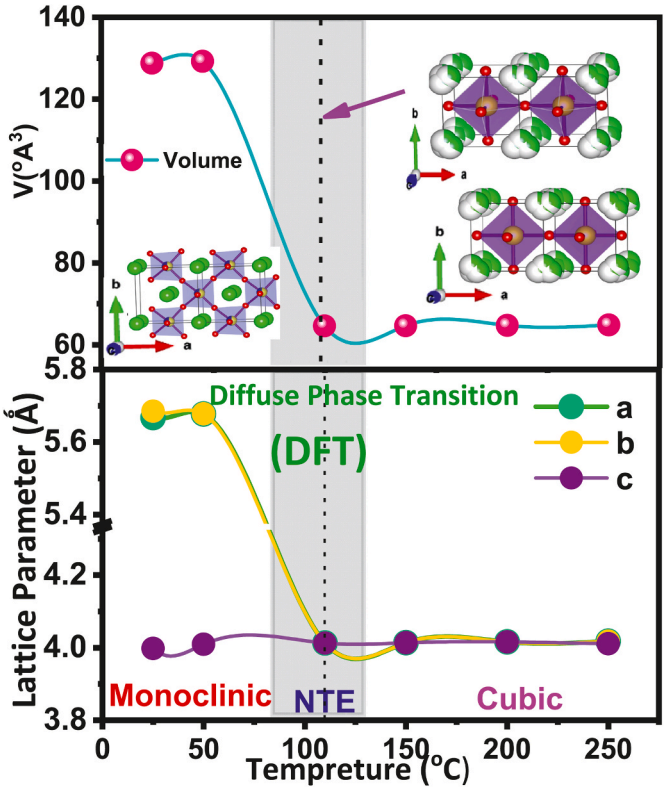

Fig. 5. Variation of Lattice parameter, volume and Negative thermal expansion (NTE) of PFN.

increase densification, thereby improving material compactness. The Optimizing density and grain size tailored for improving the properties PFN.

4.3. Dielectric and magnetic studies

The temperature dependent dielectric behaviour of PFN at different frequencies (10 Hz, 1 kHz, 100 kHz, and 1000 kHz) is shown in Fig. (a, b). The temperature dependent dielectric constant shows an increase in the dielectric constant with increasing temperature up to ~120°C and thereafter it decreases with further increase in temperature. The temperature dependent dielectric constant shows a broadening near the transition temperature (T_c). Hence PFN shows a diffuse phase transition (DPT) at the transition temperature from 105°C to 115°C. The origin of broadening in temperature dependent dielectric constant at different frequencies near the transition temperature occurs due to local fluctuations of chemical composition and long range polar nanoregions (PNRs) in the micro-areas. Further, it is related to the disorder distribution on B-side cations (Fe^{2+}/Fe^{3+} and Nb^{5+}) in the PFN perovskite unit cell, as shown in Fig. 8(c) [59–73].

The dielectric anomalous behaviour of the dielectric constant with respective temperature assigned to the structural phase transition from monoclinic to cubic structure was confirmed by the HT-XRD [Fig. 4(ii)]. The observed dielectric constant and loss of the PFN-8-3 sample are found to be 18600 and 0.01, respectively; however, for the PFN-7-2 these parameters are obtained as 1100 and 0.19, respectively. The rises in dielectric constant for the PFN-8-3 sample as compared to the PFN-7-2 are due to an increase in relative density from 80 to 98 % with time and temperature (Table 4).

The resulting PFN samples' dielectric constant maxima (ε_{rmax}) values are similarly influenced by the various sizes and shapes of the ceramic grains [Fig. 6(a and b)]. The relationship between the dielectric constant and the microstructure of materials is first understood by changing the dielectric constant values for porosity and the secondary phase. The

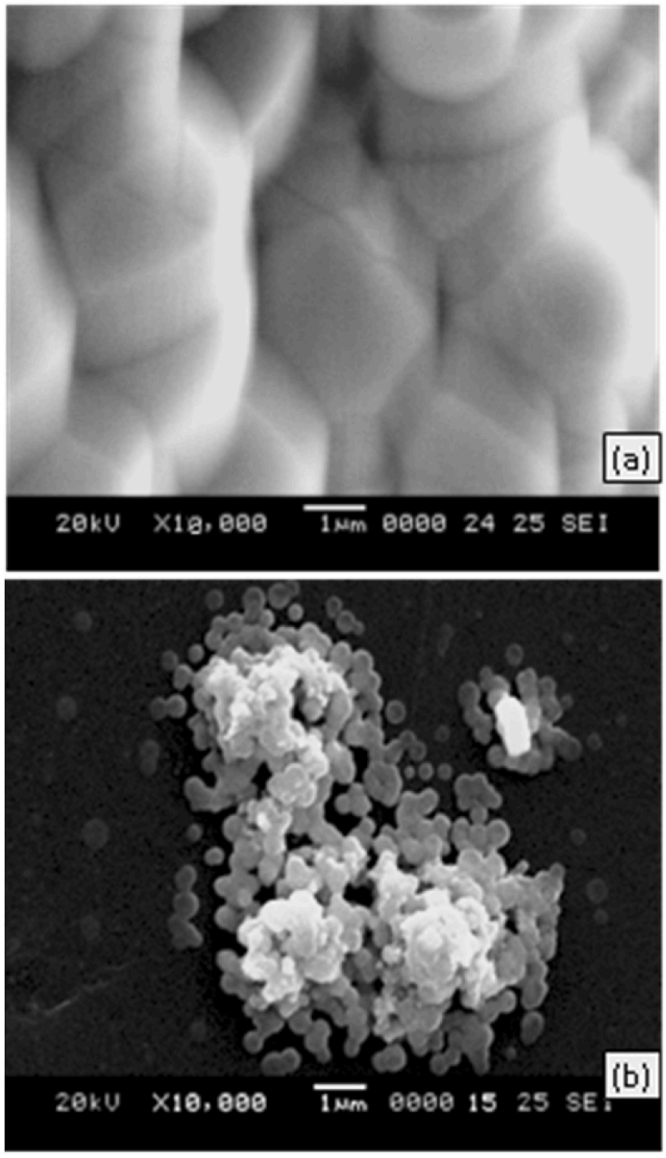

Fig. 6. SEM of as-synthesis PFN heated at (a) 500°C and (b) fracture surface of sample sintered at 800°C (PFN-8-3).

quantitative technique for correcting the porosity influence on the dielectric constant (ε_{rmax}) is explained by equation [74]. The formula developed by Rushman and Strivens are $\varepsilon_{r(Corrected)} = \frac{\varepsilon_{r(Observed)} \times (2+V_2)}{2(1-V_2)}$ where V_2 is the volume percentage of porosity in the sample and r (observed) is the observed dielectric constant. The dielectric constant that is best suited for correcting porosity below 35 % is V_2.

Fig. 9 (a & b) depicted the frequency dependent dielectric response of the PFN-7-3 and PFN-8-3 samples at various temperatures of 50, 75, 100, 125, 150, 175, and 200°C. Due to interfacial polarization, a rapid decrease in dielectric constant and loss is shown when the frequency increases from 10 Hz to 1000 kHz. The interfacial polarization is found higher at the lower frequency due to the difference in conductivity of grain and grain boundaries. However, at higher frequencies, charges enter the grain, and the grain-boundary interface layer cannot follow the probing ac-signal, causing the reduction of the dielectric constant at higher frequencies [33, 75]. From Fig. 9, PFN shows the dielectric relaxation, follows the Debye model at certain temperature and frequencies, indicating that it has a single a single characteristics relaxation time. This is observed in paraelectric phase, where thermal energy overcomes dipole interactions, and the dipoles respond more uniformly

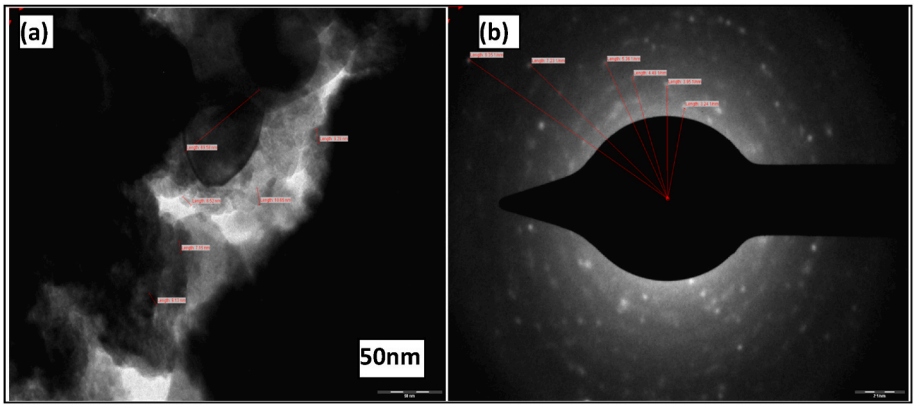

Fig. 7. TEM of (a) as-synthesized PFN heated at 250^{0}C, (b) Selected Area Electron Diffraction (SAED) patterns of random distributed polar nano regions (PNRs).

Table 3
A comparison of grain size and bulk density of PFN.

Comp	Route	Pyrochlore (%)	Grain size (nm)	Relative density (%)	Ref.
PFN	Solid state	1	2500	78	[27]
PFN	Sol-gel	1	250	90	[4]
PFN	Mechanochemical	–	800	95	[29]
PFN	Co-precipitation	–	500	–	[57]
PFN	Molten salt	3	1500	64	[58]
PFN	**Combustion route**	**0**	**<100(at 500^{0}C) <3000 (for PFN-8-3)**	**-98**	**Present study**

to the electric field. The Debye relaxation process in PFN varies with temperature. In the paraelectric phase (Above T_c), PFN may show a clear Debye-like relaxation as the dipole lose their strong correlation and begin to behave more independently, which aligns with the single

Table 4
Density correction on dielectric constant and average grainsize for PFN prepared at two different sintering temperature and time.

Sample	Vol fraction of porosity (V_2)	$\tan\delta_{max}$	ε_r (observed) 1 kHz,	ε_r (corrected) 1 kHz	Tc	Grain Size (μm)
PFN-7-2	0.20	0.19	1100	1512	115	~2
PFN-7-3	0.12	0.06	16500	19875	112	~1.8
PFN-8-2	0.10	0.5	10017	11686	90	~2.5
PFN-8-3	0.02	0.01	18600	19169	112	~3

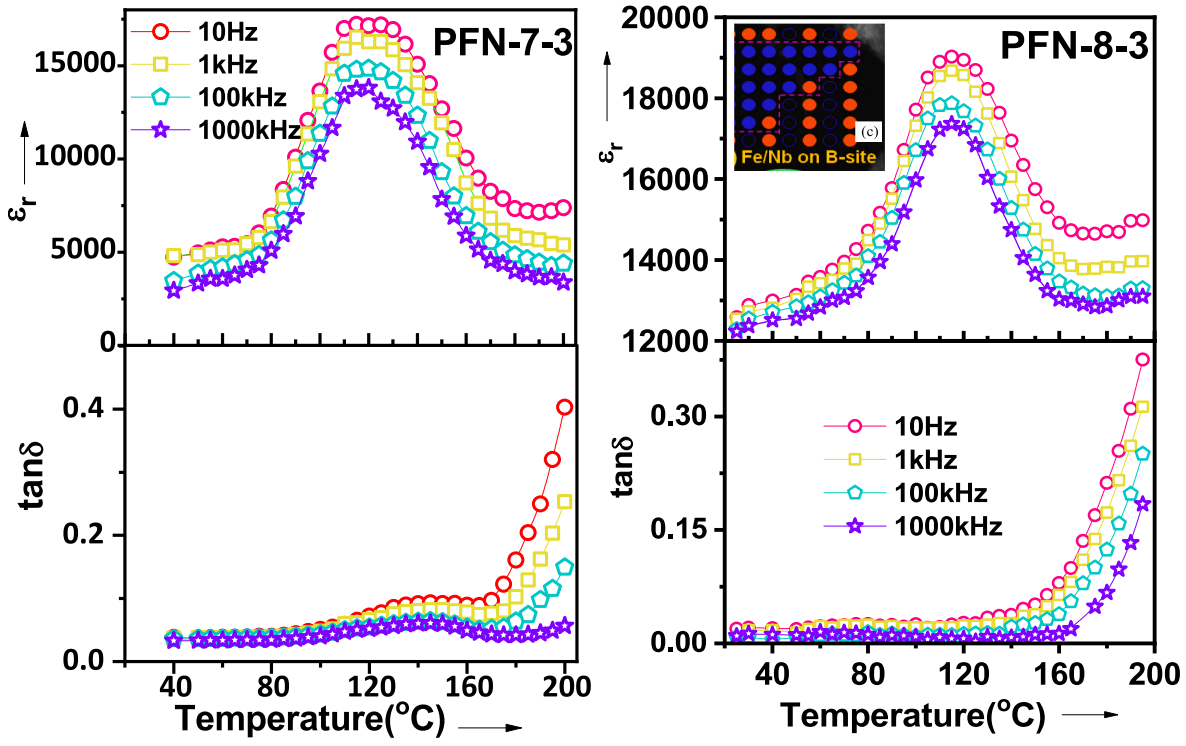

Fig. 8. Dielectric constant and loss variation with the frequency for sample (a)PFN-7-3 (b) PFN-8-3 (c) Fe/Nb on B-site of PFN.

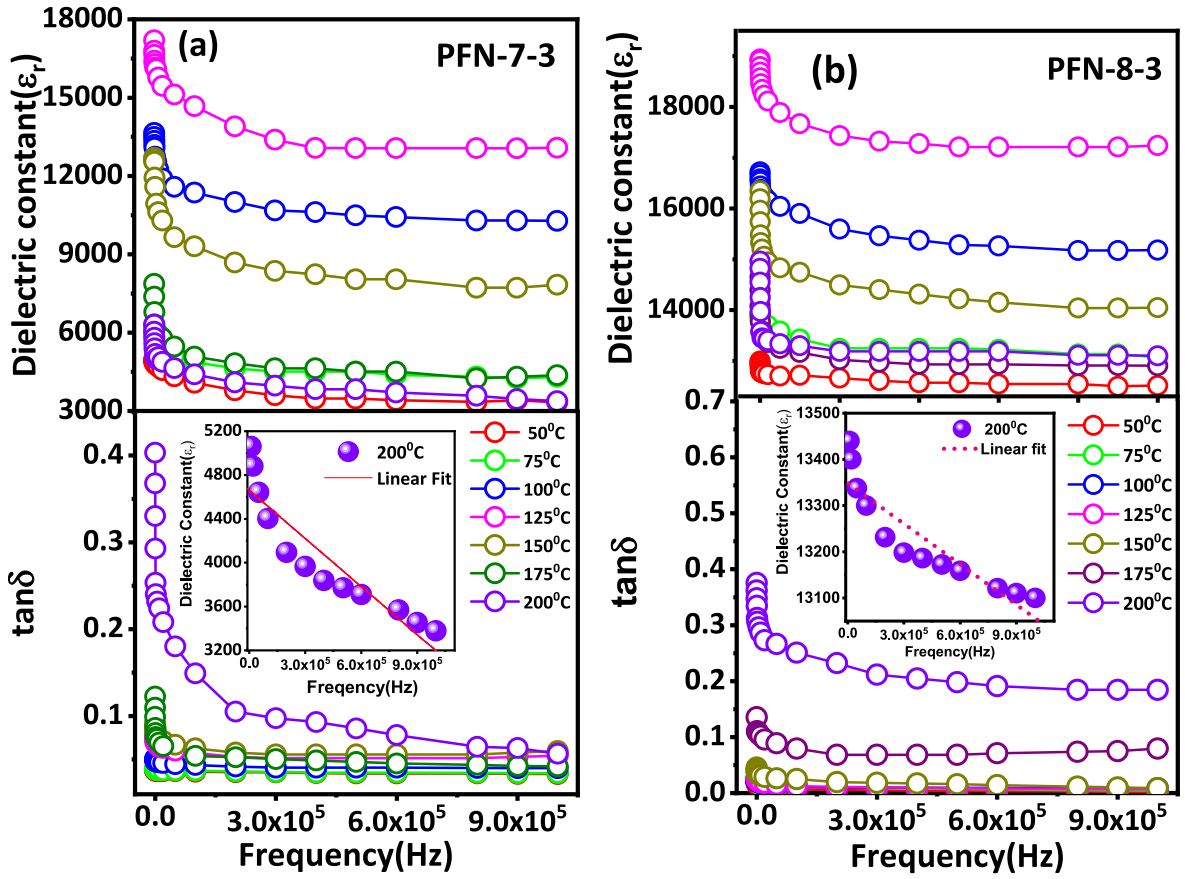

Fig. 9. Frequency dependence of the dielectric constant and loss at the 50, 75, 100, 125, 150, 175 and 200°C temperature for sample (a) PFN-7-3 and (b) PFN-8-3.

relaxation time. Such unison in the frequency response reflects in terms of frequency dependent dielectric behaviour, as shown in Fig. 9 (a & b: inset). The PFN non relaxor behaviour contributes to its Debye-like relaxation since there is less structural disorder than in relaxor materials, leading to a more uniform dipole response. The ordering of $Fe^{3+}$and Nb^{5+} ions contributes to a stable dipolar arrangement, favouring a Debye relaxation response rather than the broad, dispersive relaxation typical of relaxor.

An EG and GPAR vibrating sample magnetometer (VSM) (Model 4500) was used to examine the field dependent magnetization behaviours of the samples at room temperature. We measured the magnetization M vs. H up to ±8000 Oe for each sample in order to gain more understanding of the magnetic characteristics. The representative data for the samples annealed at 700°C and 800°C are displayed in Fig. 10, and all samples displayed hysteresis loops at 300 K (RT). Since there is reduced remnant magnetization (M_r) and magnetic susceptibility (M_s), it is evident that the ferromagnetic component of the samples rapidly increases as the calcination temperature rises starting at 800°C. Additionally, the slight variations in the coercive magnetic field (H_c) are not readily apparent. In contrast to the majority of the reports in the published literature, a magnetic measurement on calcined PFN powders is less ferromagnetic in nature even at room temperature.

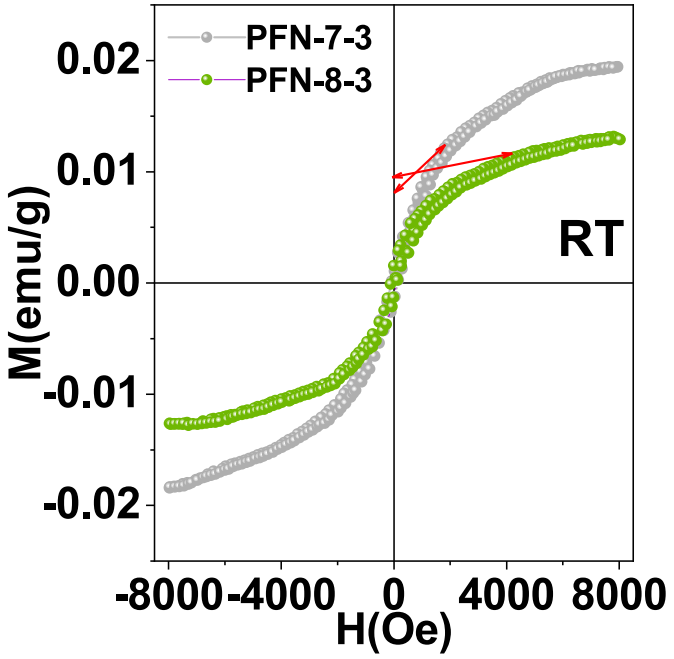

Fig. 10. Room-temperature hysteresis loops for samples annealed at 700 and 800°C at RT.

5. Conclusion

A one-step SHS approach was used to synthesize a single-phase monoclinic nano-PFN powder. Gaussian fitting of XRD and Rietveld refinement of HT-XRD data validated the monoclinic structure of PFN. It is discovered that the SHS approach yields a high yield and is easy to use. In accordance with TEM pictures and SEM confirmation, the samples include oval-shaped nanoparticle ranging in size from 10 to 50 nm. The effects of porosity, particle size, and compactness on the dielectric behavior of PFN materials were examined. The non-relaxor ferroelectric behaviour, distinguishing it from typical relaxor materials. Non-relaxor behaviour in PFN attributed to its long-range ferroelectric order and

specific structural characteristics. This non-relaxor nature of PFN due to long range order of Fe^{+3} and Nb^{5+}, PFN dielectric response remains more consistent across a range of frequencies compared to relaxor, sharp and broad phase transition and the crystal structure of PFN plays a role in its non-relaxor behavior, the arrangement of ions within its perovskite lattice contributes to the stability of the ferroelectric phase, a maintaining an ordered dipole orientation that differs from the randomly oriented dipoles in relaxor materials. This anomalous dielectric behavior was correlated with structural phase transition. PFN powders confirm its ferromagnetic nature even at room temperature. This work may pave a path for designing the ceramic and its composites with ferroic properties for various applications.

CRediT authorship contribution statement

Tanveer Quazi: Writing – original draft, Methodology, Investigation. **Shahin Sayyad:** Writing – review & editing, Investigation. **Vishwajit M. Gaikwad:** Writing – review & editing.

Ethical approval

Not applicable.

Declaration of competing interest

The authors declare that they have no known competing financial interests or personal relationships that could have appeared to influence the work reported in this paper.

Acknowledgement

Not applicable.

Data availability

The authors do not have permission to share data.

References

[1] J.C. Burfoot, G.W. Taylor, Polar Dielectric and Their Applications, University of California press, 2023, 9780520315334.
[2] R. Sobiestianskas, W. Peng, N. Leme, M. Karkut, J. Banys, J. Holc, M. Kosec, Microwave dielectric dispersion in a multiferroic $Pb(Fe_{1/2}Nb_{1/2})O_3$ thin film, Appl. Phys. Lett. 100 (2012) 122904, https://doi.org/10.1063/1.3696043.
[3] D. Bochenek, P. Guzdek, Ferroelectric and magnetic properties of ferroelectromagnetic $PbFe_{1/2}Nb_{1/2}O_3$ type ceramics, J. Magn. Magn Mater. 323 (2011) 369–374, https://doi.org/10.1016/j.jmmm.2010.09.046.
[4] S.B. Majumder, S. Bhattacharyya, R.S. Katiyar, A. Manivannan, P. Dutta, M. S. Seehra, Dielectric and magnetic properties of sol-gel-derived lead iron niobate ceramics, J. Appl. Phys. 99 (2006) 024108, https://doi.org/10.1063/1.4799414.
[5] Uroš Praha, Tadej Rojac, Magdalena Wencka, Mirela Dragomir, Andraž Bradeško, Andreja Benčan, Rachel Sherbondy, Geoff Brennecka, Zdravko Kutnjak, Barbara Malič, Hana Uršiča, Improving the multicaloric properties of Pb $(Fe_{0.5}Nb_{0.5})O_3$ by controlling the sintering conditions and doping with manganese, J. Eur. Ceram. Soc. 39 (2019) 4122–4130, https://doi.org/10.1016/j.jeurceramsoc.2019.05.062.
[6] Uro Praha, Mirela Dragomir, Tadej Rojac, Andreja Benčan, Rachel Broughton, Ching-Chang Chung, Jacob L. Jones, Rachel Sherbondy, Geoff Brennecka, Hana Uršiča, Strengthened relaxor behavior in$(1-x)Pb(Fe_{0.5}Nb_{0.5})O_3$–$xBiFeO_3$, RSC, J. Mater. Chem. C 8 (2020) 3452, https://doi.org/10.1039/c9tc05883d.
[7] R.R. Vedantam, V. Subramanian, V. Sivasubramanian, V.R.K. Murthy, Low frequency dielectric studies on $Pb(Fe_{1/2}Nb_{1/2})O_3$, Mater. Sci. Eng. B 113 (2004) 136–142, https://doi.org/10.1016/j.mseb.2004.06.018.
[8] Manfred Fiebig, Thomas Lotter Moser, Dennis Meier, Morgan Trassin, The evolution of multiferroics, Nat. Rev. Mater. 1 (2016) 16046, https://doi.org/10.1038/natrevmats.2016.46.
[9] N. A Spaldin, Multiferroics: past, present, and future, MRS Bull. 42 (2017) 385–390, https://doi.org/10.1557/mrs.2017.86.
[10] L. Christodoulou, J.D. Venables, Multifunctional material systems: the first generation, JOM (J. Occup. Med.) 55 (2003) 39–45, https://doi.org/10.1007/s11837-003-0008-z.
[11] J. Allison, D. Backman, L. Christodoulou, Integrated computational materials engineering: a new paradigm for the global materials profession, JOM (J. Occup. Med.) 58 (2006) 25–27, https://doi.org/10.1007/s11837-006-0223-5.
[12] C. Dagdeviren, P. Joe, O.L. Tuzman, K.I. Park, K.J. Lee, Y. Shi, Y. Huang, J. A. Rogers, Recent progress in flexible and stretchable piezoelectric devices for mechanical energy harvesting, sensing and actuation. Extreme Mechanics, Letture 9 (2016) 269–281, https://doi.org/10.1016/j.eml.2016.05.015.
[13] H. Elahi, M. Eugeni, P. Gaudenzi, A review on mechanisms for piezoelectric-based energy harvesters, Energies 11 (2018) 1850, https://doi.org/10.3390/en11071850.
[14] G.A. Smolenskii, Proc. 2nd meet. Of ferroelectricity, J. Phys. Soc. Jpn. 28 (1970) 26. Kyoto.
[15] I.K. Jeong, J.S. Ahn, B.G. Kim, S. Yoon, Satendra Pal Singh, D. Pandey, Short- and medium-range structure of multiferroic $Pb(Fe_{1/2}Nb_{1/2})O_3$ studied using neutron total scattering analysis, Phy. Rev. B 83 (2011) 064108, https://doi.org/10.1103/PhysRevB.83.064108.
[16] S. Matteppanavar, B. Angadi, S. Rayaprol, Single phase synthesis and room temperature neutron diffraction studies on multiferroic PbFe0.5Nb0.5O3, AIP Conf. Proc. 1512 (2013) 1232–1233, https://doi.org/10.1063/1.4791496.
[17] G.A. Smolenskii, V.A. Isupov, A.I. Agranovskaya, S.N. Popv, Soviet, Phys. Solid State 2 (1961) 2584.
[18] V.A. Bokov, I.E. Mylnikova, G.A. Smolenskii, J. Exp. Theor. Phys. USSR Phys. Ser. 42 (1962) 643.
[19] V.V. Bhat, A.M. Umarji, V.B. Shenoy, U.V. Waghmare, Diffuse ferroelectric phase transitions in Pb-substituted $Pb(Fe_{1/2}Nb_{1/2})O_3$, Phys. Rev. B 72 (2005) 014104, https://doi.org/10.1103/PhysRevB.72.014104.
[20] Y.C. Liou, C.Y. Shih, C.H. Yu, Stoichiometric $Pb(Mg_{1/3}Nb_{2/3})O_3$ perovskite ceramics produced by reaction-sintering process Mater, Letture 57 (2003) 1977–1981, https://doi.org/10.1016/S0025-5408(03)00145-4.
[21] C.C. Chiu, C.C. Li, S.B. Desu, Molten salt synthesis of a complex perovskite, Pb $(Fe_{0.5}Nb_{0.5})O_3$, J. Am. Ceram. Soc. 74 (1991) 38–41, https://doi.org/10.1111/j.1151-2916.1991.tb07293.x.
[22] T.R. Shrout, S.L. Swartz, M.J. Haun, Dielectric properties in the $Pb(Fe_{1/2}Nb_{1/2})O_3$-$Pb(Ni_{1/3}Nb_{2/3})O_3$ solid-solution system, Am. Ceram. Soc. Bull. 63 (1984) 808–820. http://pascalfrancis.inist.fr/vibad/index.php?action=getRecordDetail&idt=9002023.
[23] D. Mohan, R. Prasad, Srikumar Banerjee, Dielectric properties of lead magnesium niobate and lead iron niobate prepared by the semiwet hydroxide route, J. Am. Ceram. Soc. 84 (2001) 2126–2128, https://doi.org/10.1111/j.1151-2916.2001.tb00971.x.
[24] M. Yokosuka, Electrical and electromechanical properties of hot-pressed $Pb(Fe_{1/2}Nb_{1/2})O_3$ ferroelectric ceramics, Japan, J. Appl. Phys. 32 (1993) 1142, https://doi.org/10.1143/JJAP.32.1142.
[25] J.T. Wang, M.K. Mbonye, C. Zhang, Dielectric, piezoelectric and magnetic properties of ferroelectromagnet $Pb(Fe_{1/3}Nb_{2/3})O_3$(PFN) ceramics, Int. J. Mod. Phys. B 17 (2003) 3732, https://doi.org/10.1142/S021797920302171X.
[26] Y. Yu, C. Feng, C. Li, Y. Yang, H. Yan, Effects of processing routes on structures and dielectric properties of lead iron niobate-lead magnesium niobate binary system, Jpn. J. Appl. Phys. (40) (2001) 2348, https://doi.org/10.1143/JJAP.40.2348. Part-1.
[27] Y. Yang, J.M. Liu, H.B. Huang, W.Q. Zou, P. Bao, Z.G. Liu, Magnetoelectric coupling in ferroelectromagnet $Pb(Fe_{1/2}Nb_{1/2})O_3$ single crystals, Phys. Rev. B70 (2004) 132101, https://doi.org/10.1103/PhysRevB.70.132101.
[28] D. Mohan, R. Prasad, S. Banerjee, Dielectric properties of lead magnesium niobate and lead iron niobate prepared by the semiwet hydroxide route, J. Am. Ceram. Soc. 84 (2001) 2126, https://doi.org/10.1111/j.1151-2916.2001.tb00971.
[29] Xingsen Gao, Junmin Xue, John Wang, Ting Yu, Ze Xiang Shen, Sequential combination of constituent oxides in the synthesis of $Pb(Fe_{1/2}Nb_{1/2})O_3$ by mechanical activation, J. Am. Ceram. Soc. 85 (3) (2002) 565–572, https://doi.org/10.1111/j.1151-2916.2002.tb00133.x.
[30] Dariusz Bochenek, Przemysław Niemiec, Ferro-electromagnetic properties of $PbFe_{1/2}Nb_{1/2}O_3$ (PFN) material synthesized by chemical-wet technology, Materials 11 (12) (2018) 2504, https://doi.org/10.3390/ma11122504.
[31] S.P. Singh, A.K. Singh, D. Pandey, H. Sharma, Om Prakash, Crystallographic phases, phase transitions, and barrier layer formation in (1-x) $[Pb(Fe_{1/2}Nb_{1/2})O_3]$-$xPbTiO_3$, J. Mater. Res. 18 (2003) 2677–2687, https://doi.org/10.1557/JMR.2003.0374.
[32] A.R. West, Basic Solid-State Chemistry, second ed., John Wiley, 2014.
[33] K. Singh, S.A. Band, W.K. Kinge, Ferroelectric, 306 (2004179-2004185.https://doi.org/10.1080/00150190490460821.
[34] Y. Zhang, G.C. Stangle, Preparation of fine multicomponent oxide ceramic powder by a combustion synthesis process, J. Mater. Res. 9 (1994) 1997–2004, https://doi.org/10.1557/JMR.1994.1997.
[35] M.M.A. Sekar, A. Halliyal, K.C. Patil, Synthesis, characterization, and properties of lead based relaxor ferroelectrics, J. Mater. Res. 11 (1996) 1210–1218, https://doi.org/10.1557/JMR.1996.0155.
[36] D.A. Fumo, J.R. Jurado, A.M. Segadaes, J.R. Frade, Combustion synthesis of iron substituted strontium titanate perovskite, Mater. Res. Bull. 32 (10) (1997) 1459–1470, https://doi.org/10.1016/S0025-5408(97)00117-7.
[37] A.M. Segadaes, M.R. Morelli, R.G.A. Kiminami, Combustion synthesis of aluminum titanate, J. Eur. Ceram. Soc. 18 (7) (1998) 771–778, https://doi.org/10.1016/S0955-2219(98)00004-1.
[38] V.C. Sousa, A.M. Segadaes, M.R. Morelli, R.G.A. Kiminami, Combustion synthesized ZnO powders for varistor ceramics, Int. J. Inorg. Mater. 1 (2) (1999) 235–241, https://doi.org/10.1016/S1466-6049(99)00036-7.
[39] M.T. Colomer, D.A. Fumo, J.R. Jurdo, A.M. Segadaes, Non-stoichiometric $La_{(1-x)}NiO_{(3-\delta)}$ perovskites produced by combustion synthesis, J. Mater. Chem. 9 (1999) 2505–2510, https://doi.org/10.1039/A902808K.

[40] A.G. Merzhanov, C.N.R. Rao, in: Chemistry of Advanced Materials, IUPAC 21st Century Monograph Series, Blackwell, Oxford, 1992.

[41] S.R. Jain, K. C Adiga, V.R. Pai Verneker, A new approach to thermo chemical calculations of condensed fuel oxidizer mixture, Combust. Flame 40 (1981) 71–79, https://doi.org/10.1016/0010-2180(81)90111-5.

[42] M.P. Kassarjian, R.E. Newnham, J.U. Biggers, Reduction of losses in lead-iron niobate dielectric ceramics, Am. Ceram. Soc. Bull. 64 (1985) 1108.

[43] Evgenij Barsoukov, J.R. Macdonald, Impedence Spectroscopy, John Wiley and Sons, Inc., New York, 2005, https://doi.org/10.1002/0471716243.

[44] S.L. Swarts, T.R. Shrout, Fabrication of perovskite lead magnesium niobate, Mater. Res. Bull. 17 (1982) 1245–1250, https://doi.org/10.1016/0025-5408(82)90159-3.

[45] ASTM Standard, Annual Book of ASTM Standards, vol. 15, ASTM, Philadelphia. P. A, 1989, pp. 19103–19118, 02, C373-88, P109-110.

[46] S.P. Singh, D. Pandey, S. Yoon, S. Baikand, N. Shin, Evidence for monoclinic crystal structure and negative thermal expansion below magnetic transition temperature in $Pb(Fe_{1/2}Nb_{1/2})O_3$, Appl. Phys. Lett. 90 (2007) 242915, https://doi.org/10.1063/1.2748856.

[47] B.P. Burton, E. Cockayne, S. Tinte, U.V. Waghmare, First-principles-based simulations of relaxor ferroelectrics, Phase Transitions 79 (2006) 91, https://doi.org/10.1080/01411590500435962.

[48] K. Kimura, D. Urushihara, R. Kondo, Y. Yamamoto, A.K.R. Ang, T. Asaka, N. Happo, T. Hagihara, T. Matsushita, H. Tajiri, H. Miyazaki, K. Ohara, M. Iwata, K. Hayashi, Element-selective local structural analysis around B-site cations in multiferroic $Pb(Fe_{1/2}Nb_{1/2})O_3$ using x-ray fluorescence holography, Phys. Rev. B 104 (2021) 144101, https://doi.org/10.1103/PhysRevB.104.144101.

[49] K. Kimura, K. Yokochi, R. Kondo, D. Urushihara, Y. Yamamoto, Artoni Kevin R. Ang, N. Happo, K. Ohara, T. Matsushita, T. Asaka, Local structural analysis of Pb $(Fe_{1/2}Nb_{1/2})O_3$ multiferroic material using X-ray fluorescence holography, Jpn. J. Appl. Phys. 58 (2019) 100601, https://doi.org/10.7567/1347-4065/ab4681.

[50] S.C. Shirbhate, K. Singh, S.A. Acharya, A.K. Yadav, Review on local structural properties of ceria-based electrolytes for IT-SOFC, Ionics 23 (2017) 1049–1057, https://doi.org/10.1007/s11581-016-1893-9.

[51] S.K. Paswan, S. Kumari, M.B. Kar, A. Singh, H. Pathak, J.P. Borah, L. Kumar, Optimization of structure-property relationships in nickel ferrite nanoparticles annealed at different temperature, J. Phys. Chem. Solid. 151 (2021) 109928, https://doi.org/10.1016/j.jpcs.2020.109928.

[52] V.M. Gaikwad, S.A. Acharya, Perovskite-spinel composite approach to modify room temperature structural, magnetic and dielectric behavior of $BiFeO_3$, J. Alloys Compd. 695 (2017) 3689, https://doi.org/10.1016/j.jallcom.2016.11.367.

[53] S. Kumari, N. Ortega, A. Kumar, S.P. Pavunny, J.W. Hubbard, C. Rinaldi, Dielectric anomalies due to grain boundary conduction in chemically substituted $BiFeO_3$, J. Appl. Phys. 17 (2015) 114102, https://doi.org/10.1063/1.4915110.

[54] G. Srinivasan, J.F. Scott, R.S. Katiyar, Investigation of defect structure of impurity-doped lithium niobate by combining thermodynamic constraints with lattice constant variations, J. Appl. Phys. 117 (2015) 14102, https://doi.org/10.1063/1.4905286.

[55] I.H. Brunskill, R. Boutellier, W. Depmeier, H. Schmid, High-temperature solution growth of $Pb(Fe_{0.5}Nb_{0.5})O_3$ and $Pb(Mn_{0.5}Nb_{0.5})O3$ crystals, J. Crysr. Growth 56 (1982) 541–546, https://doi.org/10.1016/0022-0248(82)90037-9.

[56] I.H. Brunskill, H. Schmid, P. Tissot, The characterization of high temperature solution-grown single crystals of $Pb(Fe_{1/2}Nb_{1/2})O_3$, Ferroelectrics 37 (1981) 547–550, https://doi.org/10.1080/00150198108223482.

[57] Jianlan Tang, Mankang Zhu, Tao Zhong, YudongHou, Hao Wang, Hui Yan, Synthesis of fine $Pb(Fe_{0.5}Nb_{0.5})O_3$ perovskite powders by coprecipitation method, Mater. Chem. Phys. 101 (2007) 475–479, https://doi.org/10.1016/j.matchemphys.2006.08.006.

[58] Kyung Bong Park, K.I. Hyun Yoon, Reaction mechanisms in the formation of perovskite $Pb(Fe_{1/2}Nb_{1/2})O_3$ by molten salt synthesis method, Ferroelectrics 132 (1992) 1–8, https://doi.org/10.1080/00150199208009066.

[59] L.E. Cross, S. Jang, R.E. Newnham, S. Nomura, K. Uchino, Large electrostrictive effects in relaxor ferroelectrics, Ferroelectrics 23 (1980) 187, https://doi.org/10.1080/00150198008018801.

[60] Guangyong Xu, Z. Zhong, Y. Bing, Z.-G. Ye, G. Shirane, Electric-field-induced redistribution of polar nano-regions in a relaxor ferroelectric, Nat. Mater. 5 (2006) 134–140, https://doi.org/10.1038/nmat1560.

[61] Shahin Sayyad, S. Acharya, Low temperature synthesis of complex solid solution $(1-x)Bi_{0.5}Na_{0.5}TiO_3$-$xBaTiO_3$ system: BT induced structural and dielectric anomalies in NBT, Ferroelectrics 537 (2018) 112–132, https://doi.org/10.1080/00150193.2018.1528950.

[62] G. Burns, F.H. Docola, The observation of glassy polarization behavior in crystalline ferroelectric materials, Ferroelectrics 52 (1) (2011) 103–113, https://doi.org/10.1080/00150198308208243.

[63] G. Burns, F.H. Docola, Crystalline ferroelectrics with glassy polarization behaviour, Phys. Rev. B 28 (1983) 2527–2530, https://doi.org/10.1103/PhysRevB.28.2527.

[64] I.K. Jeong, T.W. Darling, J.K. Lee, T. Proffen, R.H. Heffner, J.S. Park, K.S. Hong, W. Dmowski, T. Egami, Direct observation of the formation of polar nano regions in $Pb(Mg_{1/3}Nb_{2/3})O_3$ using neutron pair distribution function analysis, Phys. Rev. Lett. 94 (14) (2005) 147602, https://doi.org/10.1103/PhysRevLett.94.147602.

[65] O. Svitelskiy, J. Toulouse, G. Yong, Z.G. Ye, Polarized Raman study of the phonon dynamics in $Pb(Mg_{1/3}Nb_{2/3})O_3$ crystal, Phys. Rev. B 68 (10) (2003) 104107, https://doi.org/10.1103/PhysRevB.68.104107.

[66] J. Toulouse, F. Jiang, O. Svitelskiy, W. Chen, Z.G. Ye, Temperature evolution of the relaxor dynamics in Pb $(Zn_{1/3}Nb_{2/3})O_3$: a critical Raman analysis, Phys. Rev. B 72 (18) (2005) 184106, https://doi.org/10.1103/PhysRevB.72.180502.

[67] B. Mihailova, R.J. Angel, A.M. Welsch, J. Zhao, J. Engel, C. Paulmann, M. Gospodinov, H. Ahsbahs, R. Stosch, B. Güttler, U. Bismayer, Pressure-induced phase transition in $PbSc_{0.5}Ta_{0.5}O_3$ as a model Pb-based perovskite relaxor ferroelectric, Phys. Rev. Lett. 101 (2008) 017602, https://doi.org/10.1103/PhysRevLett.101.017602.

[68] B. Dkhil, P. Gemeiner, A. Al-Barakaty, L. Bellaiche, E. Dul'kin, E. Mojaev, M. Roth, Intermediate temperature scale T* in lead-based relaxor systems, Phys. Rev. B 80 (2009) 064103, https://doi.org/10.1103/PhysRevB.80.064103.

[69] D. La-Orauttapong, J. Toulouse, J.L. Robertson, Z.G. Ye, Diffuse neutron scattering study of a disordered complex perovskite Pb(Zn1/3Nb2/3)O3 crystal, Phys. Rev. B 64 (21) (2001) 212101, https://doi.org/10.1103/PhysRevB.64.212101.

[70] R. Blinc, A. Gregorovic, B. Zalar, R. Pirc, V.V. Laguta, M.D. Glinchuk, 207Pb NMR study of the relaxor behavior in Pb(Mg1/3Nb2/3)O3, Phys. Rev. B63 (2001) 024104, https://doi.org/10.1103/PhysRevB.63.024104.

[71] A.A. Bokov, Z.G. Ye, Universal relaxor polarization in and related materials, Phys. Rev. B 66 (2002) 064103, https://doi.org/10.1103/PhysRevB.66.064103.

[72] A.A. Bokov, Z.G. Ye, Double freezing of dielectric response in relaxor Pb(Mg1/3Nb2/3)O3 crystals, Phys. Rev. B 74 (2006) 132102, https://doi.org/10.1103/.74.132102.

[73] Xiao Liu, Yuyin Wang, Wenchao Tian, Fangyuan Zhu, Jicong Wang, Weijia Wang, Yanrui Li, Kaizhu Zeng, Jing Shi, Strong interfacial interaction in polarized ferroelectric heterostructure nanosheets for highly efficient and selective photocatalytic CO2 reduction, small. https://doi.org/10.1002/.202409801, 2025.

[74] D.F. Rushman, M.A. Strivens, The Effective Permittivity of Two-phase Systems, Proc. Phys. Soc, 1947, https://doi.org/10.1088/0959-5309/59/6/312, 5.

[75] Charles Evans, Richard Brundle, Wilson Jr Shaun Wilson, Encyclopedia of Materials Characterization: Surface, Interface, Thin Film, Elsevier, 1992.